



CSST Dense Star Field Preparation: A Framework for Astrometry and Photometry for Dense Star Field Images Obtained by the China Space Station Telescope (CSST)

Yining Wang¹, Rui Sun¹, Tianyuan Deng¹, Chenghui Zhao², Peixuan Zhao², Jiayi Yang², Peng Jia^{1,3}, Huigen Liu², and Jilin Zhou²
¹College of Electronic Information and Optical Engineering, Taiyuan University of Technology, Taiyuan 030024, China; robinmartin20@gmail.com
²School of Astronomy & Space Science, Nanjing University, Nanjing 210093, China; huigen@nju.edu.cn
³Peng Cheng Lab, Shenzhen 518066, China

Received 2023 December 23; revised 2024 March 2; accepted 2024 May 17; published 2024 July 8

Abstract

The China Space Station Telescope (CSST) is a telescope with 2 m diameter, obtaining images with high quality through wide-field observations. In its first observation cycle, to capture time-domain observation data, the CSST is proposed to observe the Galactic halo across different epochs. These data have significant potential for the study of properties of stars and exoplanets. However, the density of stars in the Galactic center is high, and it is a well-known challenge to perform astrometry and photometry in such a dense star field. This paper presents a deep learning-based framework designed to process dense star field images obtained by the CSST, which includes photometry, astrometry, and classifications of targets according to their light curve periods. With simulated CSST observation data, we demonstrate that this deep learning framework achieves photometry accuracy of 2% and astrometry accuracy of 0.03 pixel for stars with moderate brightness $\text{mag} = 24$ (i band), surpassing results obtained by traditional methods. Additionally, the deep learning based light curve classification algorithm could pick up celestial targets whose magnitude variations are 1.7 times larger than magnitude variations brought by Poisson photon noise. We anticipate that our framework could be effectively used to process dense star field images obtained by the CSST.

Key words: techniques: photometric – methods: data analysis – astrometry

1. Introduction

The China Space Station Telescope (CSST) is China's cutting-edge space telescope, with a 2 m aperture and a field of view (FOV) exceeding 1.1 square degrees.⁴ The CSST is designed to observe from near-ultraviolet to optical band, delivering a remarkable point-spread function (PSF) with the radius of 80% energy concentration (R_{EE80}) smaller than $0''.15$. With an unparalleled combination of a large FOV and high spatial resolution, the CSST anticipates making groundbreaking discoveries. One of its potential scientific projects is a time-domain survey of the Galactic center, conducting observations over several weeks. The time-domain survey focuses on dense star fields, providing an unprecedented level of spatial resolution and temporal cadence. The observational data will encompass light curves and positions for millions of stars. These light curves hold paramount importance, offering insights into the nature, structure, composition, and evolution of celestial objects. Characteristic features within light curves of diverse phenomena, including supernovae, Cepheid variables, and eclipsing binaries, enable astronomers to measure

cosmic distances, refine cosmological models, and probe the internal structure and nuclear processes of stars. Furthermore, periodic variability in light curves is pivotal for the detection and study of transiting exoplanets, as well as understanding the rotational dynamics of asteroids and comets.

Prior to deriving any further scientific insights, our initial phase involves obtaining positions and magnitudes of celestial objects and subsequently identifying potential celestial object candidates based on the time-domain data of the magnitudes and positions. As is widely acknowledged, we face three significant challenges during the process: the detection of celestial objects, the photometry analysis of these objects, and the classification of celestial objects based on their light curve patterns. Due to the subpar performance of classical detection and photometry methods in the dense star fields observed by CSST, both detection and photometry are susceptible to interference from neighboring targets. The study carried out in this paper primarily seeks to assess the effectiveness of various detection and photometry techniques, encompassing classical detection methods (Bertin & Arnouts 1996), the PSF photometry approach, and machine learning based detection and photometry methods (PNet, Sun et al. 2023).

⁴ https://csst-tb.bao.ac.cn/code/csst_sim/csst-simulation

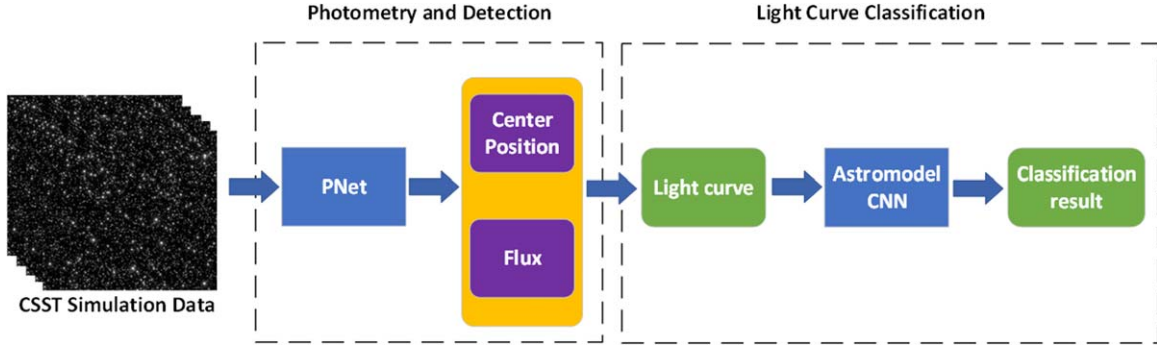


Figure 1. Framework for astrometry, photometry, and light curve classification of dense star field images obtained by CSST.

In our pursuit of uncovering the potential advantages and disadvantages of different photometry and detection approaches, we further employ a deep learning based light curve classification method. The light curve classification problem has been widely discussed in different papers. Building upon existing knowledge, Strobe et al. (2010) started on a comprehensive investigation of nova light curves. They initiated observations and detailed analyses, encompassing both graphical and tabular representations of their findings. This study not only documented several key attributes, including peak brightness and corresponding dates, but also significantly advanced our understanding of the morphological characteristics and properties of nova light curves. The advancement of machine learning techniques has seen a growing trend in utilizing these algorithms for light curve classification. Richards et al. (2011) employed Random Forest classifiers for this purpose, Hinnert et al. (2018) utilized bidirectional Long Short-Term Memory Recurrent Neural Networks (bidirectional LSTM RNNs) as a representation learning method for prediction and classification of Kepler light curves. Similarly, Olmschenk et al. (2024) employed Convolutional Neural Networks (CNNs) to efficiently identify short-period variable stars in the Transiting Exoplanet Survey Satellite (TESS) all-sky image data. In this work, we present an improved astromodel-based CNN (Shallue & Vanderburg 2018; Yu et al. 2019) This CNN is integrated into our framework for light curve classification (Basri et al. 2010). Compared to the CNN network model in the Olmschenk et al. (2024) work, the CNN model presented in this paper incorporates auxiliary features in addition to light curve inputs with the aim of enhancing its classification accuracy.

In summary, this paper proposes a detection, photometry and light curve classification framework for a dense stellar field observed by the CSST as diagrammed in Figure 1. In dense star fields, traditional photometry and detection algorithms are more prone to interference from neighboring targets, thus affecting the accuracy of photometry and detection. However, the PNet model integrated in our framework significantly enhances the

precision and recall rate of the results. Furthermore, when integrated with the deep learning based light curve classification algorithm, our framework obtains an improved accuracy of light curve classification results. The paper is structured as follows. In Section 2, we outline the methodology for generating time-domain observation data of the dense star field obtained by the CSST. Section 3 details the design of the deep learning based pipeline for detecting and measuring magnitudes of celestial objects within dense star fields, as well as the classical method for performance comparison. In Section 4, we present the light curve classification algorithm used in this paper, which can effectively identify celestial objects that exhibit periodic magnitude variations. Based on the detection capability, photometry accuracy, and light curve classification results, we will estimate the potential of the CSST in discovering celestial objects with periodic magnitude variations. Finally, in Section 5, we draw our conclusions and outline prospects for our future endeavors.

2. Simulation of the CSST Dense Star Field Observation Data

In this section, we show the process of generating a catalog for a specific sky region of interest and simulating observation images obtained by the CSST. Within a target sky area spanning 0.01 square degrees and centered at coordinates R.A. $17^{\text{h}} 56^{\text{m}} 51^{\text{s}}$, decl. $-29^{\text{d}} 34^{\text{m}} 45^{\text{s}}$ (J2000), situated in the halo near the bulge region, we utilize galaxy model TRILEGAL (Vanhollebeke et al. 2009) and Gaia Data Release 3 (DR3) data to construct the input catalog for generation of simulated images. To ensure the completeness of our input data, we consider the decreasing completeness of Gaia DR3 data (Cantat-Gaudin et al. 2023) in dim stars and keep stars in the input catalog with G magnitude less than 20. Additionally, we calculate the magnitude of the average flux density in the g and i bands for the TRILEGAL data to maintain consistency with the Gaia G magnitudes. We also ensure that the fraction of average magnitudes greater than 20 is retained in the TRILEGAL data. It is worth noting that parameters such as

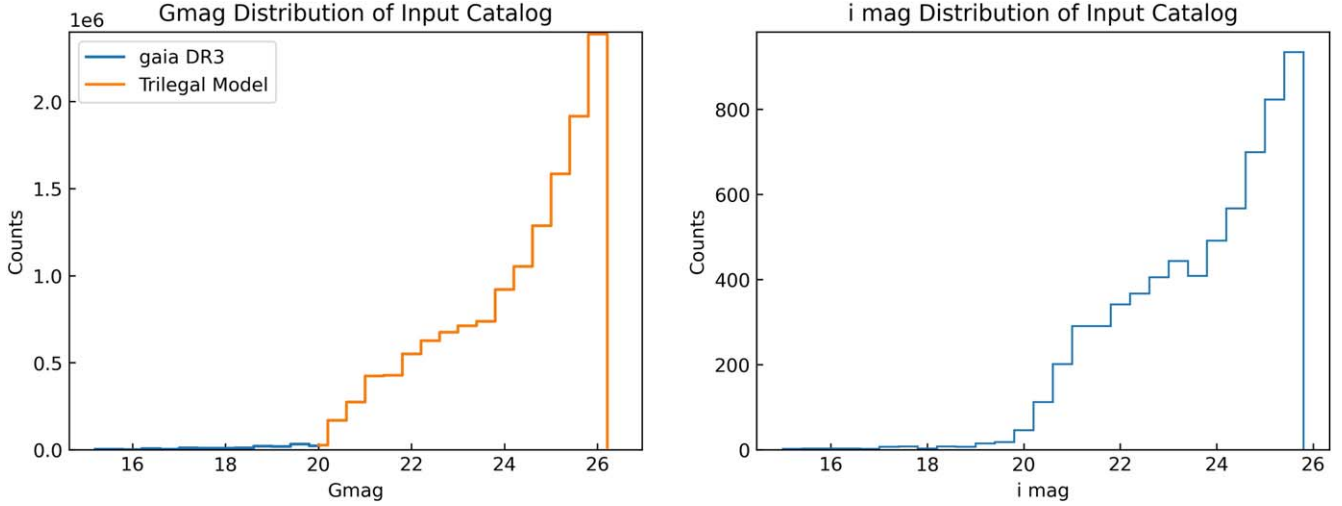


Figure 2. The distribution of stars with different magnitude within the target region. As demonstrated in left panel, the distribution of stars keeps a coherent pattern between the Gaia catalog and TRILEGAL model. Right panel shows the corresponding i band distribution obtained by CSST simulation code within a 500×500 pixel region, and all below analysis are based on i band simulation image.

stellar density remain relatively stable within the target region, allowing us to expand the catalog data to cover 0.792 square degrees, corresponding to the FOV of 18 chips (u , g , r , i , z , y , NUV) of the CSST.

To validate the effectiveness of the preceding work, we present several figures depicting parameter distributions, as detailed below. In Figure 2, the G band magnitude distribution clearly exhibits a coherent pattern around a magnitude of 20. Prior research (Wang et al. 2023) has indicated that when $m_i = 16$, the photometry signal-to-noise ratio (S/N) reaches approximately 600, after considering jitter noise. A straightforward algorithm yields photometry precision of 1% at $m_i = 22$, which is sufficient for detecting a hot Jupiter. Considering a limiting magnitude around 25.9 in i band, we have established a cut-off at $m_G = 26$, although it is possible to set a higher limiting magnitude in the TRILEGAL model. Furthermore, we have estimated the number of background galaxies, which is less than 1% of all stars, therefore, we neglect the background galaxies.

The stellar physical characteristics within the target region are depicted in Figures 3 and 4. Approximately 87% of the stars fall within the main sequence. The distribution of spectral types is detailed in Table 1. It is also worth mentioning that M-type stars only account for 5%, due to the limiting magnitude setting not being sufficiently high. We employ the CSST simulation code to generate simulated images,⁵ taking into account instrumental effects such as dark currents and readout noise. As our goal is to analyze time-domain observation data, we generate time series images, based on time variable catalogs, including eclipsing binaries, variables

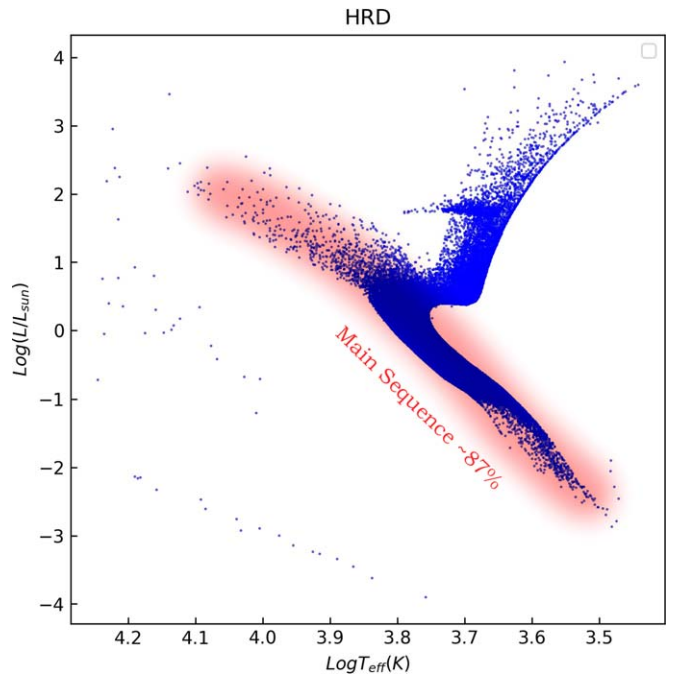


Figure 3. The Hertzsprung–Russell (H-R) diagram of stars in the catalog. As displayed in this figure, around 87% of all stars are main sequence stars.

and transiting exoplanets with fractions of 1%, 0.02%, and 1%, respectively. The periods of eclipsing binaries satisfy a Gaussian distribution (Duquennoy et al. 1991), while the other two are consistent with a uniform distribution within 1.45 to 2.95 days. Finally, we simulate 1000 images captured in the i -band with an exposure time of 300 seconds per frame, resulting

⁵ https://csst-tb.bao.ac.cn/code/csst_sim/csst-simulation

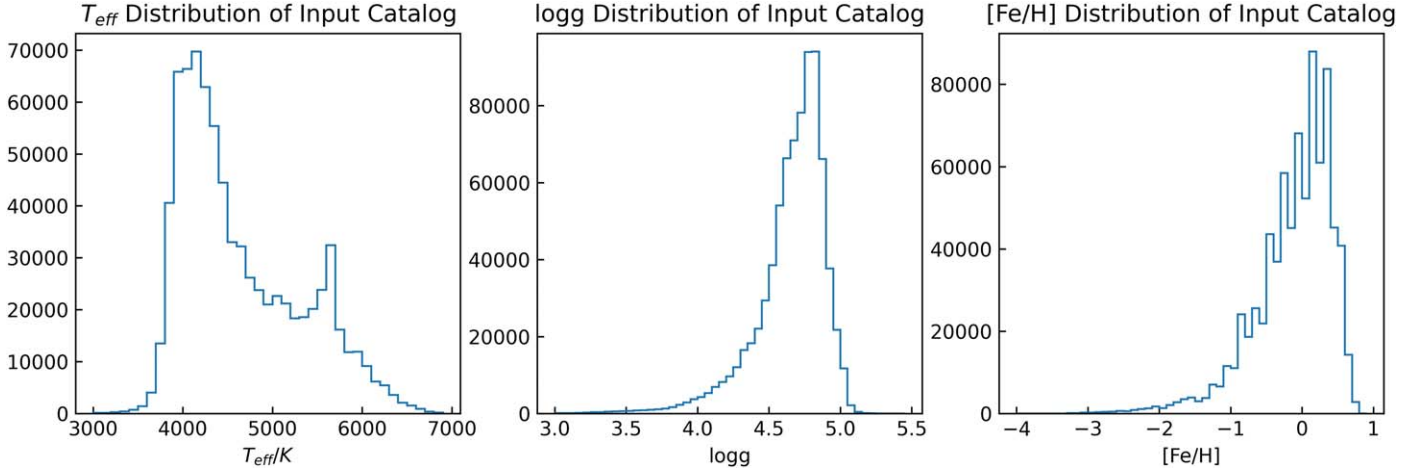


Figure 4. The distribution of effective temperature, surface gravity and metal abundance of stars in the simulated data, from left to right respectively.

Table 1

The Distribution of the T_{eff} Interval (Pecaut & Mamajek 2013) and Percentage of Stars with Different Spectral type in Simulated Data

Spectral Type	M	K	G	F
T_{eff}	<3865	3865–5310	5310–5980	5980–7320
Proportion	5%	73%	16%	4%

Note. For a typical M-type star, considering $L \sim 0.04L_{\odot}$, $d \sim 8$ kpc, and an extinction coefficient around 2–3 mag, we can assess that at i magnitude of 26, the M-type star is just starting to show up, which explains the small fraction of the M-types quantitatively.

in a data set of 1000 frames (the time spanning is about 3.5 days) that will be used for subsequent analysis.

3. The Data Processing Framework for CSST Dense Star Field Observations

Processing data from a dense star field presents a known data processing challenge, characterized by three key difficulties. First, the high density of stars within the field makes it particularly challenging to distinguish individual stars from the observational data due to overlapping. Second, the measurement of a single star’s flux is significantly influenced by its proximity to neighboring stars. Third, errors stemming from the detection and photometry steps pose a considerable obstacle to the effectiveness of the light curve classification algorithm. Therefore, it is imperative to assess the performance of various methods and develop a comprehensive end-to-end framework for processing dense star field observational data obtained by the CSST.

In this section, we will introduce both the traditional method and the deep learning based algorithm for identifying and conducting photometric measurements on stars within dense star fields. We will evaluate the performance of these two approaches and select the most suitable method for

constructing the framework. Additionally, as scientists require the identification of interesting targets, such as flare events, binaries, or exoplanets, for further investigation, we have incorporated a deep learning based light curve classification algorithm into the framework. In summary, the framework described in this section assists scientists in generating catalogs from each observation image and in identifying celestial objects with periodic light curves for subsequent analysis. Further details of the framework will be discussed below.

3.1. Classical Target Detection and Photometry Algorithm for Dense Star Fields

3.1.1. Classical Target Detection Algorithm

Typically, scientists employ classical algorithms for both detection and photometry tasks. One commonly utilized software for these purposes is Source Extractor (SExtractor). SExtractor identifies celestial objects by detecting local peaks in brightness and consolidates these detection results to produce the final results (Bertin & Arnouts 1996). In scenarios with sparsely populated star fields, SExtractor performs admirably, effectively identifying a majority of stars. However, in denser star fields, the intricacy of target detection increases, and the performance of SExtractor may be affected. Consequently, we continuously fine-tune parameters of SExtractor based on its performance tested with simulated data. The final configuration we adopt is detailed in Table 2.

3.1.2. Classical Photometry Algorithm

Two classical photometry methods are commonly used: aperture photometry and PSF photometry. Aperture photometry is typically used for processing images of sparse star fields. It involves employing a fixed-size aperture to calculate the flux of celestial objects. On the other hand, PSF photometry

Table 2
Parameters for SExtractor

Parameter Name	Value	Description
DETECT TYPE	CCD	CCD (linear) or PHOTO (with gamma correction)
DETECT MINAREA	3	min. # of pixels above threshold
DETECT THRESH	1.6	$\langle \text{sigmas} \rangle$ or $\langle \text{threshold} \rangle$, $\langle ZP \rangle$ in mag arcsec ⁻²
ANALYSIS THRESH	10	$\langle \text{sigmas} \rangle$ or $\langle \text{threshold} \rangle$, $\langle ZP \rangle$ in mag arcsec ⁻²
DEBLEND NTHRESH	60	Number of deblending sub-thresholds
DEBLEND MINCONT	0.001	Minimum contrast parameter for deblending

is a technique used for measuring the brightness of stars in astronomical images by fitting the light distribution with the PSF (Stetson 1987; Starck et al. 1998). PSF photometry can be applied to both dense and sparse star fields. However, it necessitates stable observation conditions and prior knowledge of PSFs, making it more suitable for images acquired by space telescopes (Holtzman 1990; Anderson & King 2006). Past studies have demonstrated the successful application of PSF photometry to data obtained by the Hubble Space Telescope (Dolphin & Kennicutt 2002; Holtzman et al. 2006; Garcia et al. 2015). Given the observation conditions of the CSST, we propose to use PSF photometry in this study.

We adhere to the standard PSF photometry procedures for preprocessing the observational data. Initially, we partition the observation images into smaller units, each comprising 100 by 100 pixels. Subsequently, we apply a smoothing filter and compute the median values within each unit as estimates for the sky background. Finally, we subtract the sky background from the observation images. These processed images are then forwarded to the PSF photometry algorithm for magnitude estimation. In the PSF photometry algorithm, we fit the PSF provided by the simulation code with images of celestial objects and calculate the flux of celestial objects with Equation (1)

$$\text{flux} = \iint \text{PSF}(x, y) \cdot I(x, y) \, dx \, dy, \quad (1)$$

where $\text{PSF}(x, y)$ represents the normalized grey scale values of celestial objects in different positions defined by the PSF model, and $I(x, y)$ denotes the brightness distribution of the target. The target flux and magnitude are then converted using the formula

$$\text{mag} = -2.5 \log_{10}(\text{flux}) + b, \quad (2)$$

where the constant b is obtained through flux calibration.

3.2. Deep Learning Based Target Detection and Photometry Algorithm—PNet

3.2.1. The Structure of PNet

In recent years, deep learning has experienced rapid growth and has been applied in various domains, including natural language processing, image recognition, and image classification. Among

these applications, deep learning has been extensively explored in the realm of target detection algorithms. This exploration encompasses two-stage detection algorithms such as Fast R-CNN (Girshick 2015), Faster R-CNN (Ren et al. 2015), and Cascade R-CNN (Cai & Vasconcelos), as well as single-stage detection algorithms such as YOLO (Redmon et al. 2016), SSD (Liu et al. 2016) and RetinaNet (Lin et al. 2017). The principles underpinning these target detection algorithms in the field of computer vision align with those of target detection and photometry algorithms in astronomical image analysis. They share the common goal of determining the positions of celestial objects and calculating their properties. However, when dealing with celestial objects, we often need to perform regression to estimate their magnitudes, whereas general purpose target detection algorithms primarily focus on classifying objects. Building on this concept, numerous deep learning-based target detection algorithms have found extensive applications in astronomy. For instance, Faster R-CNN has been employed for astronomical target detection and classification in wide-field small-aperture telescopes (Jia et al. 2020), while YOLO has been used for the detection and identification of galaxies (González et al. 2018).

To meet the demands of precise photometry and effective detection of celestial objects in dense star-field images, we have chosen to employ PNet in this study (Sun et al. 2023). PNet is a deep learning neural network, which is developed for detection, astrometry, and photometry of celestial objects, leveraging the framework proposed in Jia et al. (2020). The architecture of PNet is illustrated in Figure 5. The initial image undergoes a feature extraction process within a neural network to generate feature maps. Following this, a fully convolutional analysis network processes these feature maps, determining the central positions of stars and relevant flux-related data. PNet is built upon CenterNet (Zhou et al. 2019) and incorporates a specialized photometry branch. To tailor it for star detection and measurement, certain adjustments have been implemented. For more comprehensive information regarding PNet, we refer readers to the original paper (Sun et al. 2023). Given that PNet was originally designed for processing images of sparse star fields obtained by ground-based time-domain surveys, which are quite different from the dense star fields discussed in this

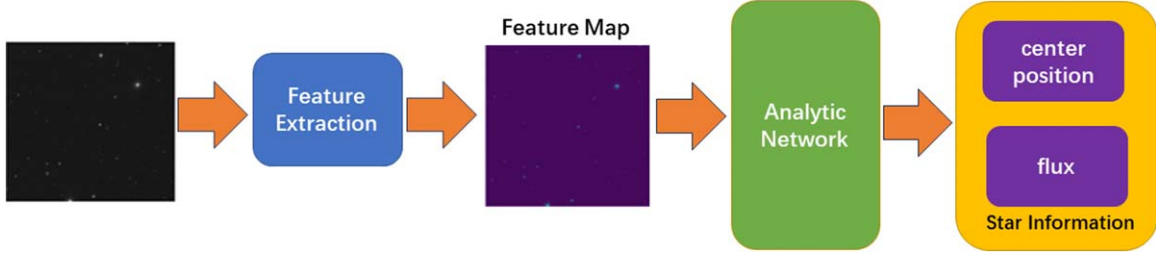


Figure 5. The architecture of PNet.

paper, we have implemented specific adjustments to tailor PNet for our purposes. First, we have removed the downsampling module. In dense star field images, pixels corresponding to different stars tend to merge into a single pixel, if we apply the downsampling module. While this modification does increase computational demands, it notably bolsters PNet’s capability to detect and measure objects in dense star fields. Second, to ensure high-precision magnitude calculations, we have transitioned the neural network’s precision from half precision floating point numbers to single precision floating point numbers. Despite the augmented computational resources required, this adjustment results in a more stable training process and increased accuracy in magnitude measurements.

3.2.2. Training of PNet

As simulating time-domain observation images demands substantial computational resources, we only create observation images for a single sky area as mentioned in Section 2. This region contains 5000×5000 pixels with a pixel scale of 0.074 pixels per arcsec. A total of 631,475 stars are contained in the simulated images. We have produced 1000 images of this sky area and each of them are captured at different epochs. Subsequently, we have subdivided the sky area into stamp images, each sized at 128×128 pixels. Notably, 98.69% of these stamp images are earmarked for the training data set, while the remaining 1.31% constitute the test data set. The latter comprises 4038 stars for evaluation. Due to the faintness of targets with magnitudes of 25 and above, they are not taken into consideration during network training and detection. When validating the detection and photometric accuracy of the neural network for individual images, we use the entire image as the test set to ensure an adequate amount of data.

Based on our experience, achieving convergence with PNet is challenging due to its two distinct branches, particularly the photometry branch, which requires an extensive amount of time for convergence. As a result, we employ a transfer learning strategy during the training phase. We utilize pre-trained weights provided by Sun et al. (2023) and further train the neural network with the Focal Loss (Lin et al. 2017) as the loss function for target detection. The Focal Loss defined in this

Table 3
Hardware Specifications Used in Our Study

Parameter Name	Value
GPU	GeForce RTX 3090 \times 3
CPU	Intel(R) Xeon(R) Silver 4210R CPU @ 2.40 GHz
GPU Memory	24 GB \times 3
RAM	256 GB
CUDA Version	11.7
CuDNN Version	8.6
PyTorch Version	1.10.0+cu11.3

paper is expressed in Equation (3),

$$\text{FocalLoss}(p_t) = -\alpha_t(1 - p_t)^\gamma \log(p_t), \quad (3)$$

where α_t is the weighting factor used to adjust the weights of positive and negative samples, p_t is the output of the network, and $\gamma > 0$ is an adjustable focusing parameter. We set γ as 2 in this paper. With the focal loss, we can obtain a balance of detection abilities between bright and dim targets. We further use the Mean Absolute Error (MAE) loss and the Mean Square Error (MSE) loss to evaluate the astrometry and photometry error. The MAE is used to estimate astrometry error, while the MSE loss is used to evaluate photometry error. They are defined in Equation (4),

$$\begin{aligned} \text{MAE} &= \frac{1}{n} \sum_{i=1}^n |\hat{y}_i - y_i| \\ \text{MSE} &= \frac{1}{n} \sum_{i=1}^n (\hat{\text{mag}}_i - \text{mag}_i)^2. \end{aligned} \quad (4)$$

The Focal Loss, MAE and MSE will be added together as a loss function for PNet. With the loss function defined above, we further employ the Adam Optimizer (Kingma & Ba 2014) to train the neural network. The neural network is trained in a computer with configurations defined in Table 3 and it will take approximately 10 minutes to train the neural network with batch size of 10. After approximately 200 epochs of training, the network achieved an acceptable performance in detection, astrometry and photometry of celestial objects.

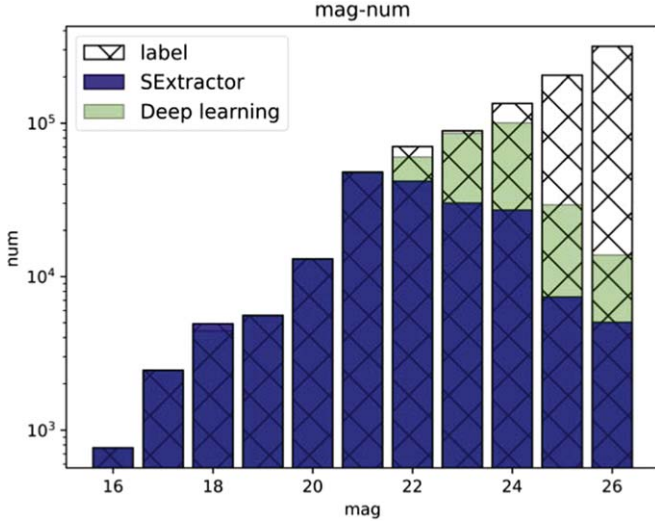


Figure 6. The number of celestial objects detected by different methods. As shown in this figure, our method has better ability in detection of dim targets.

3.3. Performance Comparison between the Classical Method and the Deep Learning Based Method

In this section, we will assess the performance of both the classical method and the deep learning based method in detection and photometry of celestial objects. To cross-check the detection results, we set the centering error threshold as 0.1 pixels. This implies that we will consider detection results as true positives if the distance between their positions and the ground-truth positions is less than 0.1 pixels. Subsequently, we will evaluate the magnitudes of the detected targets and compare them to the ground-truth magnitude values. These results will serve as the basis for comparing these two methods. Further details regarding these results will be discussed below.

3.3.1. Comparison of the Detection Abilities

We first compare the detection capabilities of these two methods. The number of detected targets is depicted in Figure 6. As illustrated in this figure, there is not a significant disparity in performance between these two detection methods for bright targets (with magnitudes ranging from 14 to 20). However, when it comes to dim and densely distributed targets, the deep learning based method outperforms the classical approach. To provide a more comprehensive assessment, we have calculated both the *recall rate* and *precision rate* for each of these methods. The *recall rate* is defined as the number of true positives divided by the sum of true positives and false negatives. The *precision rate* is defined as the percentage of true positive predictions among all positive predictions made by the model. The classical method achieves a *recall rate* of 51% and a *precision rate* of 83%, whereas PNet boasts a *recall rate* of 89.9% and a *precision rate* of 95%. The *F1 score* is the

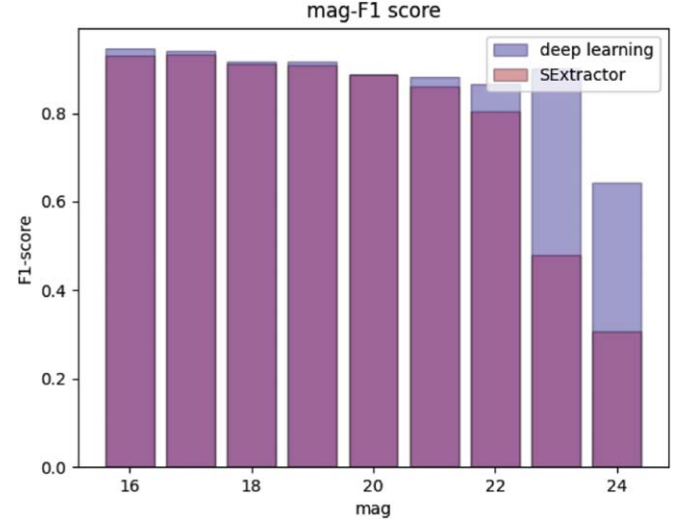


Figure 7. The *F1 score* of different methods. As shown in this figure, our method has higher *F1 score* in detection of dim targets.

harmonic mean of precision and recall, which can be used as a direct evaluation criterion for the detection algorithm. The *F1 score* for the classical method is 0.635, while the *F1 score* for PNet is 0.924. As shown in Figure 7, the *F1 score* of PNet is significantly larger than that of the classical method, particularly for dim stars.

3.3.2. Comparison of the Photometry Abilities

In dense star fields, where stars are close to each other, PSF photometry encounters challenges. This is because, when stars are in close proximity, the PSF photometry tends to over-estimate magnitudes. This occurs because the PSF photometry fits the PSF for each candidate and derives their magnitudes and photons from nearby stars, which will introduce noises to photometry results. In contrast, PNet is capable of learning complex functions to estimate the magnitudes of stars with varying spatial distributions. For instance, considering that PNet processes the entire image with multiple spatial scales, in cases where stars are in close proximity, the PNet can identify nearby stars and determine magnitudes using distinct strategies tailored to specific situations. This capability helps mitigate the influence of nearby stars on photometry results, ultimately enhancing the accuracy of photometry.

As depicted in Figure 8, the photometry results obtained by PNet surpass those of PSF photometry, indicating that the estimated magnitudes closely align with the true values. The mean error for the PSF photometry results is 0.399 mag, whereas the mean error for the PNet is 0.055 mag. These results signify the capability of PNet to deliver more consistent and stable photometry results for dense star fields. Furthermore, we illustrate the variance in photometry results obtained by PNet and the PSF photometry method in Figure 9. As shown in

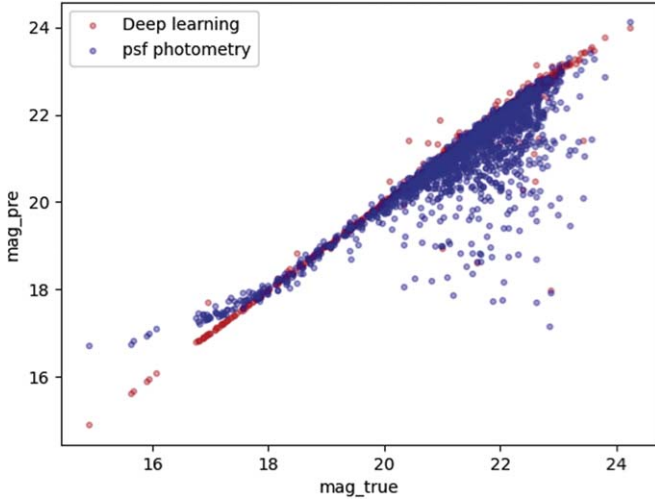


Figure 8. The distribution of photometry errors for stars of varying magnitudes is presented in this figure. It is evident that PNet consistently provides more consistent and stable photometry results, while the PSF photometry method tends to yield comparatively less accurate results. Specifically, the PSF photometry method often overestimates magnitudes for the majority of stars, a phenomenon driven by the influence of nearby sources, while simultaneously underestimating magnitudes for brighter stars.

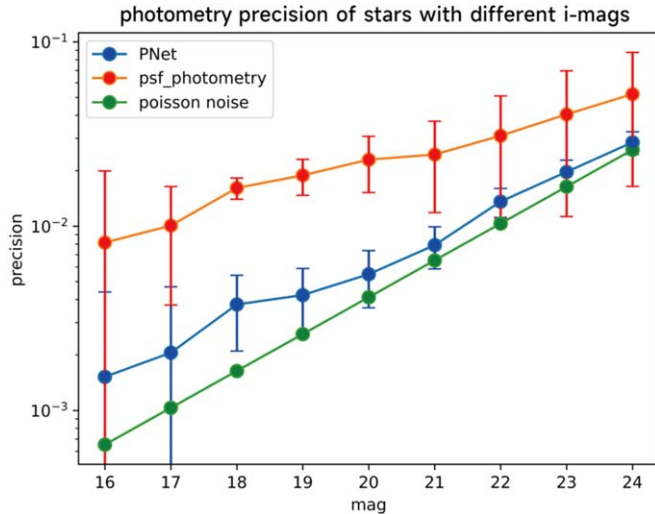


Figure 9. The distribution of standard deviation of photometry results obtained by different methods is depicted in this figure. It is evident that PNet yields more consistent and stable photometry results. For stars brighter than 16, the precision could be smaller than 7×10^{-4} and is not shown in this figure.

this figure, PNet achieves a photometry error as low as 0.001–0.003 mag for stars with magnitudes ranging from 17 to 20. Even for fainter stars, PNet continues to provide reliable results, with a photometry error of approximately 0.43 mag for stars with a magnitude of 23.5.

4. The Light Curve Classification Algorithm

By conducting detection and photometry on 1000 sets of simulated time-domain images from the CSST, we can obtain light curves for celestial objects. These light curves provide direct evidence for the identification of various types of celestial objects, facilitating further exploration. Light curve classification is a crucial area of research in astronomy, focused on categorizing and studying changes in the brightness of celestial objects over time (Mandel & Agol 2002; Tey et al. 2023). These variations can result from internal processes like stellar pulsations, eruptions, and rotations, as well as external factors such as gravitational interactions between celestial bodies, matter accretion, and collisions. The analysis of light curves offers valuable insight into the structure, evolution, physical mechanisms, and interactions of celestial objects. To enhance our understanding and categorization of different types of light curves, astronomers have developed various methods and criteria. The primary goal of light curve classification is to group and compare these curves based on their distinctive features and behaviors, enabling a deeper understanding of their physical characteristics and evolutionary processes. These classification approaches often consider aspects like curve shape, periodicity, duration, and amplitude.

In this paper, our primary focus is on a specific and straightforward scenario known as macro-classification. Here, our objective is to assess the effectiveness of our pipeline. In this particular context, we aim to categorize celestial objects based on the periodic variations observed in their light curves. To be more precise, we group binaries, stars with exoplanets, and variable stars into the “variable stars” category. Meanwhile, all other stars, including those with flare events or longer-period magnitude variations that extend beyond the observation epochs, are classified as “non-periodic variable stars.” To accomplish this task, we employ a deep learning based algorithm for light curve classification. To rigorously evaluate the algorithm’s performance, we execute the pipeline to obtain the final results. These results are then compared with the input catalog to determine the accuracy and recall rate of the pipeline. In this evaluation process, a star that is detected and correctly classified in terms of periodicity is considered a true positive classification case. Cases where a non-target is mistakenly identified as a star or a star with constant magnitude is misclassified as a variable star are designated as false positive classification cases. Stars exhibiting true periodic variability but not effectively detected are categorized as false negatives, while all other stars are classified as true negatives. Further elaboration on these aspects will follow in the subsequent discussion.

4.1. The Data Preprocessing Step

Data preprocessing stands as a critical initial step in the analysis of light curve data. This essential process involves refining and reformatting the raw data to ensure that subsequent analysis is both accurate and meaningful. In their raw form, light curve data

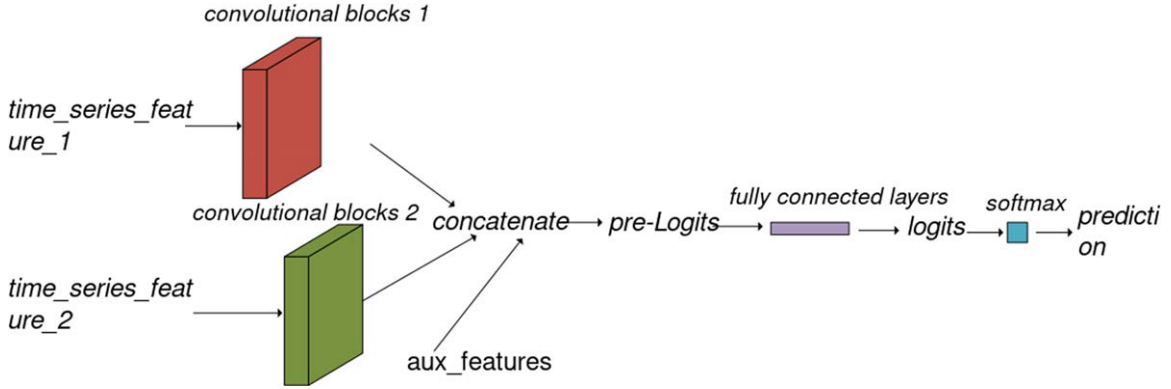


Figure 10. The structure of the CNN for light curve classification.

can often exhibit issues such as missing values or outliers. To address these concerns, we implement a series of procedures. First, we apply the 3σ rule to identify and manage outliers, utilizing linear interpolation techniques to fill in any gaps resulting from missing values. Subsequently, we standardize the light curve by normalizing it in relation to the peak magnitude value.

Additionally, we employ a median filter to enhance the quality of their light curves and fold the data according to their periods calculated by the BLS algorithm (Kovács et al. 2002; Hartman & Bakos 2016). To accommodate the requirements of our deep learning algorithm, which demands inputs of a fixed size, we uniformly sample the light curve to create a vector of consistent dimensions. We divide the light curve into two components: a global view, consisting of 201 data points, and a local view, comprising 61 data points. This division is essential for the subsequent light curve classification algorithm. Ultimately, we compile all data into a CSV file, which includes not only the light curve data but also critical details that could be obtained from other sources, such as spectral type of star, period, eclipse depth, and duration of the light curve. This consolidated file serves as the input data set for our neural network.

4.2. The Light Curve Classification Model

We employ a deep neural network proposed within the Astromodel (Shallue & Vanderburg 2018; Yu et al. 2019) for light curve classification. The Astromodel represents a versatile framework designed for defining models utilized in the analysis of astronomical data. Within this context, we leverage the Astromodel to formulate a straightforward CNN tailored for light curve classification. The structural layout of this neural network can be found in Figure 10. It adeptly processes both the light curve data and celestial target information by utilizing a hierarchical convolutional structure. Below, we present both the input and output of this light curve classification neural network:

1. First input: Zero or more time series features (e.g., light curves)

2. Second input: Zero or more auxiliary features (e.g., orbital period, transit duration)
3. Output: An integer feature with two possible values (0 = variable stars, 1 = non-periodic variable stars)
4. Output: The predicted probabilities for each class.

The input of the neural network consists of several components, including the time series data, which comprise both the global and local views of the aforementioned light curves. Additionally, this input incorporates supplementary details such as period and duration. As a light curve passes through a convolutional block, it is transformed into a one-dimensional tensor, which can be concatenated with the other information. Subsequently, a pre-logits operation is executed, encompassing various processes like activation functions and normalization techniques to fine-tune the distribution of data for optimal transmission to the fully connected layer. Following this, the input features are mapped to the output results via the fully connected layer. Ultimately, this layer outputs logits, which are then utilized in conjunction with a sigmoid classifier to facilitate the classification process and generate the final classification results.

4.3. Analysis of Light Curve Classification Results

In this section, we train the light curve classification models with light curves separately obtained by PNet and the classical method. The light curve classification model with PNet is used as a deep learning based pipeline, while the light curve classification model with the classical method is used to build a classical pipeline. The cross-entropy function is used as a loss function and we use the Adams method as the optimization algorithm for the light curve classification algorithm. After training, we use the light curves from the test set to test the performance of our algorithm. The results are shown in Figure 11. As affirmed by this figure, results obtained by PNet have higher *precision* (around 97.6%) and higher *recall rate* (around 93%), while results obtained by the classical method are relatively low.

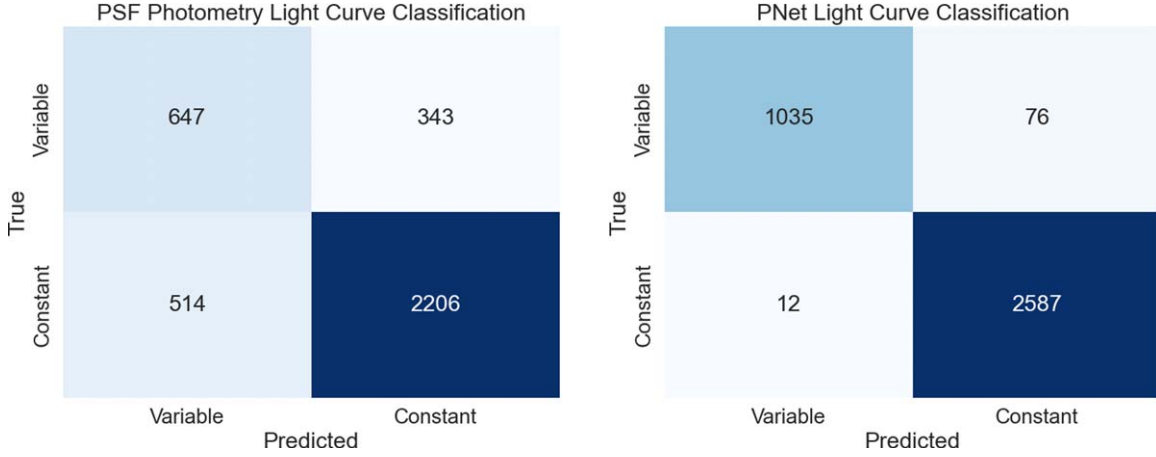


Figure 11. The confusion matrix for light curve classification obtained by two different frameworks. The left panel shows the confusion matrix obtained by the classical method, while the right panel displays the confusion matrix obtained by PNet. As affirmed by this figure, PNet with the light curve classification algorithm could obtain better results for further scientific research.

We step forward to examine the classification outcomes for various celestial objects. In this study, we have considered four distinct categories of targets: stars hosting transiting exoplanets, binary systems, variable stars, and stars with consistent brightness. To clarify, we categorize stars with fixed periods as “periodic variable stars,” while other stars fall into the “non-periodic variable stars” category. Therefore, stars hosting transiting exoplanets, binary systems, and variable stars are classified as “periodic variable stars,” whereas the rest are classified as “non-periodic variable stars.” For periodic variable stars, the distinction between magnitude variations caused by photon noise and those resulting from astronomical events significantly impacts the classification outcomes. We establish the theoretical S/N of a light curve as the ratio between the power (rms) (assuming it follows a Poisson distribution) and the variations caused by astronomical events

$$S/N = \frac{\text{Power of Signal}}{\text{Power of Noise}}. \quad (5)$$

In the case of variable stars and binary systems, the classification accuracy on CSST data can reach 97% under different noise levels. However, for transits, due to their relatively smaller amplitude variations, classification becomes more challenging, leading to a reduction in the overall classification accuracy. Figure 12 provides the classification accuracy of transits under different noise levels. As depicted in this figure, the classification accuracy is lower than 0.2, when the S/N is below 1.7. However, when the S/N is larger than 2, the classification accuracy could reach 95%.

To better investigate the difference between light curve classification results obtained by different methods, we have also identified a subset of light curves. These light curves are accurately classified by the deep learning-based pipeline but are misclassified by the classical method in Figure 13. From the

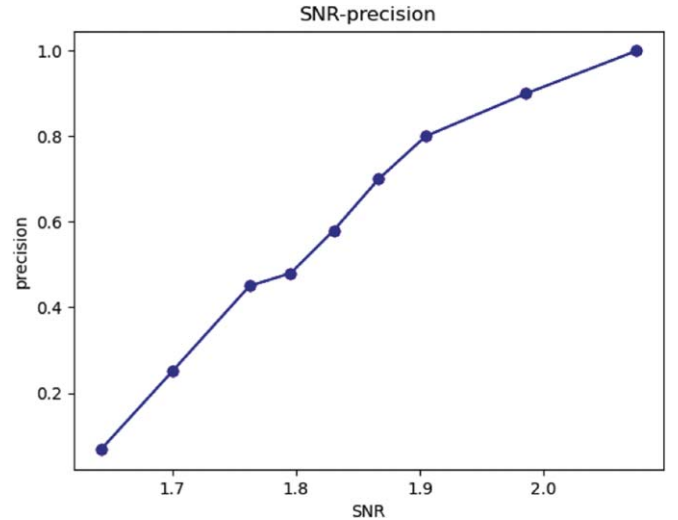


Figure 12. The classification accuracy of transit under different noise levels by the light curve classification algorithm.

figure, it can be seen that PNet is capable of more accurately fitting the variations in light curves compared to the classical PSF fitting photometry method. It also performs better in mitigating the influence of nearby variable stars in dense star fields. These findings emphasize that the deep learning-based pipeline can more effectively capture star magnitudes, especially in noisy conditions. They suggest that we can expect strong performance in processing data obtained by the CSST by the deep learning-based pipeline.

5. Discussions and Future Works

This paper presents a novel framework that demonstrates superior performance in photometry and target detection within dense stellar fields, alongside enhanced accuracy in light curve

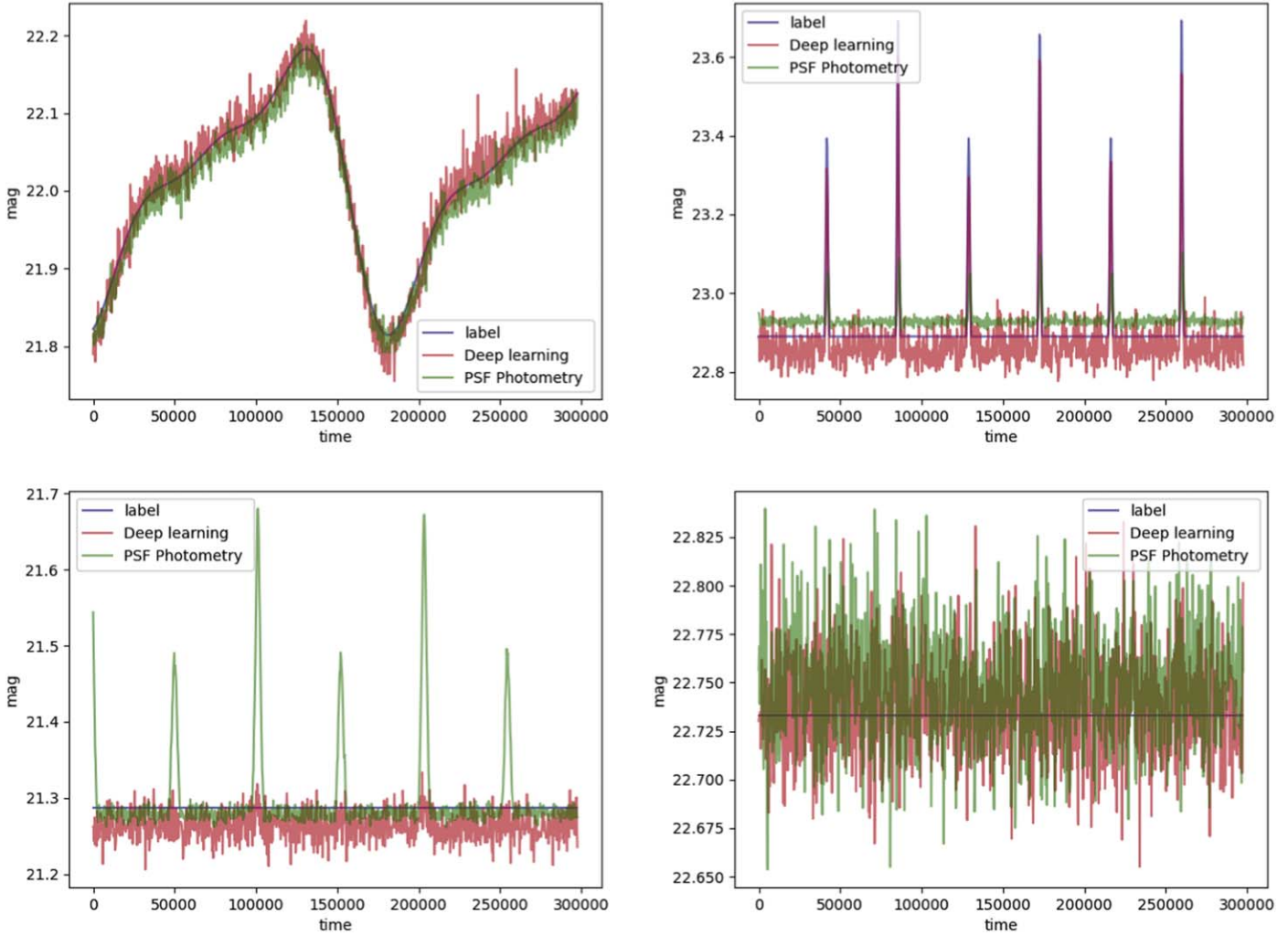


Figure 13. Theoretical light curves and those obtained through both PNet and the classical method are illustrated in this figure. As demonstrated, PNet outperforms in capturing celestial object magnitudes, leading to increased precision and recall rates in classification. A particularly intriguing case is shown in the bottom-left panel of the figure, which displays photometry results for a star situated near a variable star. In this scenario, PNet was able to successfully determine the magnitudes of the stars. For stars exhibiting variations in magnitude, the deep learning method (PNet) could more accurately depict these variations, as evidenced in the top panel of the figure. The bottom-right figure presents a star without magnitude variations, demonstrating that PNet can provide accurate results, while the PSF photometry method yields a light curve with periodic variations.

classification. We have achieved photometry accuracy of 2% and astrometry accuracy of 0.03 pixels for stars with moderate brightness $\text{mag} = 24$ (i band). We assessed our classification precision by introducing eclipsing binaries, variables, and transiting exoplanets with periods up to and including 3.5 days into the CSST simulated data. At S/N lower than 1.7, it was observed that neither classical algorithms nor deep learning techniques could deliver reliable light curve classifications. At S/N above 1.7, we attained a light curve classification accuracy of 85.5%. Leveraging these improvements in photometry, target detection, and light curve classification, we present an estimate of the number and types of different periodic variable stars detectable by the CSST. We only consider three different

types of periodic variable stars: stars hosting transiting exoplanets, eclipsing binaries, and variable stars (such as RR Lyrae stars and Cepheid stars) with periods shorter than the observation epochs. Our results can be applied to predict the survey fruits of CSST using our methods, including transiting hot Jupiters, eclipsing binaries, and variable stars.

1. Stars hosting hot Jupiters: Stars hosting hot Jupiters are a specific class of exoplanets with transiting depth around 1%, which is possibly detectable by the CSST. Belezny’s analysis of data from the TESS telescope revealed that, for stars similar to our Sun, the occurrence rate of hot Jupiters is roughly 1% (Belezny &

Kunimoto 2022). However, due to geometric detection efficiency, only about 3% of these hot Jupiters can be detected (Zhu et al. 2018). Furthermore, the occurrence rate of hot Jupiters is strongly correlated with the stellar metallicity (Wang & Fischer 2015; Zhu et al. 2016). In our simulation, we simply assume that the fraction of stars hosting hot Jupiters in the Galactic center is similar to that in the TESS FOV. Given that 87% of our star samples are main-sequence stars, if the survey sustains as long as 20 days, we estimate that there are approximately 80 hot Jupiters capable of producing detectable transiting signals within our data set of 300,000 stars, including ~ 68 hot Jupiters that can be verified by our method.

2. Binaries: The Kepler space telescope conducted observations of around 200,000 stars during its mission. Within these observations, Kepler successfully identified 2920 eclipsing binary systems, with 2098 of them having orbital periods shorter than 10 days (Kirk et al. 2016). To estimate the presence of eclipsing binary systems in our star sample, we make an extrapolation based on Kepler's findings. This extrapolation suggests that there are approximately $300,000 \times (2,098/200,000) \sim 3,150$ such binary systems within our star sample.
3. Observable variable stars (RR Lyrae stars and Cepheid stars in this paper): In contrast to the Kepler telescope, which primarily focuses on solar-type main sequence stars within a restricted FOV, the TESS space telescope conducts observations of stars of all types across the entire celestial sphere. This wide coverage provides valuable data for estimating the proportion of variable stars. Within the two-cadence data collected by TESS, 118 RR Lyrae stars were identified in Sectors 1 and 2 (Molnár et al. 2022), and 25 Cepheid stars were detected across Sectors 1–5 (Plachy et al. 2021). Given that the TESS mission observes approximately 15,000 stars in each sector, we can make a rough estimate of the fractions of RR Lyrae stars and Cepheid stars as 0.39% and 0.033%, respectively. This estimation leads us to conclude that there are at least several thousand variable stars within our star sample.

However, it is worth noting that there may be some stars that are incorrectly classified as periodic variable stars, necessitating additional human vetting through either a public science platform or other algorithms. Overall, the combined use of deep learning-based detection and photometry neural networks, along with the light curve classification algorithm, has yielded promising results in our study. This framework can be employed to process observation data from the CSST, and our research group is currently utilizing it to process real observation data to further assess its performance.

Acknowledgments

We express our gratitude for the financial support provided by the National Natural Science Foundation of China (NSFC, grant Nos. 12173027, 11973028, 11933001, 1803012, 12150009, and 12173062) and the National Key R&D Program of China (2019YFA0706601), as well as the Major Key Project of PCL. We also acknowledge the science research grants received from the China Manned Space Project with Nos. CMS-CSST-2021-B12, CMS-CSST-2021-B09 and CMS-CSST-2021-A01 and the Square Kilometre Array (SKA) Project with No. 2020SKA0110102. Additionally, we extend our appreciation to the Civil Aerospace Technology Research Project (D050105).

References

- Anderson, J., & King, I. R. 2006, PSFs, Photometry, and Astronomy for the ACS/WFC, Instrument Science Report ACS 2006-01/779-788, 34
- Basri, G., Walkowicz, L. M., Batalha, N., et al. 2010, *AJ*, **141**, 20
- Beleznyay, M., & Kunimoto, M. 2022, *MNRAS*, **516**, 75
- Bertin, E., & Arnouts, S. 1996, *A&AS*, **117**, 393
- Cantat-Gaudin, T., Fouesneau, M., Rix, H.-W., et al. 2023, *A&A*, **669**, A55
- Dolphin, A. E., & Kenicutt, R. C. 2002, *AJ*, **123**, 207
- Duquennoy, A., & Mayor, M. 1991, *A&A*, **248**, 485
- Garcia, E. V., Dupuy, T. J., Allers, K. N., Liu, M. C., & Deacon, N. R. 2015, *ApJ*, **804**, 65
- Girshick, R. 2015, in Proc. IEEE Int. Conf. on Computer Vision, 1440 (Santiago: IEEE)
- González, R. E., Muñoz, R. P., & Hernández, C. A. 2018, *A&C*, **25**, 103
- Hartman, J. D., & Bakos, G. Á. 2016, *A&C*, **17**, 1
- Hinners, T. A., Tat, K., & Thorp, R. 2018, *AJ*, **156**, 7
- Holtzman, J. A. 1990, *PASP*, **102**, 806
- Holtzman, J. A., Afonso, C., & Dolphin, A. 2006, *ApJS*, **166**, 534
- Jia, P., Liu, Q., & Sun, Y. 2020, *AJ*, **159**, 212
- Kingma, D. P., & Ba, J. 2014, arXiv:1412.6980
- Kirk, B., Conroy, K., Prša, A., et al. 2016, *AJ*, **151**, 68
- Kovács, G., Zucker, S., & Mazeh, T. 2002, *A&A*, **391**, 369
- Lin, T.-Y., Goyal, P., Girshick, R., He, K., & Dollár, P. 2017, arXiv:1708.02002
- Liu, W., Anguelov, D., Erhan, D., et al. 2016, in Computer Vision—ECCV 2016: 14th European Conf. Proc., Part I 14 (Berlin: Springer), 21
- Mandel, K., & Agol, E. 2002, *ApJL*, **580**, L171
- Molnár, L., Bódi, A., Pál, A., et al. 2022, *ApJS*, **258**, 8
- Olmschenk, G., Barry, R. K., Ishitani Silva, S., et al. 2024, arXiv:2402.12369
- Pecaut, M. J., & Mamajek, E. E. 2013, *ApJS*, **208**, 9
- Plachy, E., Pál, A., Bódi, A., et al. 2021, *ApJS*, **253**, 11
- Redmon, J., Divvala, S., Girshick, R., & Farhadi, A. 2016, in Proc. IEEE Conf. on Computer Vision and Pattern Recognition (New York: IEEE), 779
- Ren, S., He, K., Girshick, R., & Sun, J. 2015, arXiv:1506.01497
- Richards, J. W., Starr, D. L., Butler, N. R., et al. 2011, *ApJ*, **733**, 10
- Shallue, C. J., & Vanderburg, A. 2018, *AJ*, **155**, 94
- Starck, J.-L., Murtagh, F. D., & Bijaoui, A. 1998, Image Processing and Data Analysis: The Multiscale Approach (Cambridge: Cambridge Univ. Press)
- Stetson, P. B. 1987, *PASP*, **99**, 191
- Strope, R. J., Schaefer, B. E., & Henden, A. A. 2010, *AJ*, **140**, 34
- Sun, R., Jia, P., Sun, Y., et al. 2023, *AJ*, **166**, 235
- Tey, E., Moldovan, D., Kunimoto, M., et al. 2023, *AJ*, **165**, 95
- Vanhollebeke, E., Groenewegen, M. A. T., & Girardi, L. 2009, *A&A*, **498**, 95
- Wang, J., & Fischer, D. A. 2015, *AJ*, **149**, 14
- Wang, W. H., Liu, H. G., & Zhou, J. L. 2023, *AcASn*, **64**, 45
- Yu, L., Vanderburg, A., Huang, C., et al. 2019, *AJ*, **158**, 25
- Zhou, X., Wang, D., & Krähenbühl, P. 2019, arXiv:1904.07850
- Zhu, W., Petrovich, C., Wu, Y., Dong, S., & Xie, J. 2018, *ApJ*, **860**, 101
- Zhu, W., Wang, J., & Huang, C. 2016, *ApJ*, **832**, 196